Key Points:
- New deep-sea system captures time-series velocities and temperatures of diffuse flow
- Diffuse heat output from a crack was 3.1 ± 2.5 kW and estimated for all ASHES cracks 2.05 ± 1.95 MW
- Semidiurnal heat flux variability due primarily to tidal pressure variations

Supporting Information:
- Supporting Information S1

Correspondence to:
E. Mittelstaedt,
emittelstaedt@uidaho.edu

Diffuse venting at the ASHES hydrothermal field: Heat flux and tidally modulated flow variability derived from in situ time-series measurements

Eric Mittelstaedt[1], Daniel J. Fornari[2], Timothy J. Crone[3], James Kinsey[2], Deborah Kelley[4], and Mitch Elend[4]

[1]Department of Geological Sciences, University of Idaho, Moscow, Idaho, USA, [2]Department of Geology and Geophysics, Woods Hole Oceanographic Institution, Woods Hole, Massachusetts, USA, [3]Department of Marine Geology and Geophysics, Lamont-Doherty Earth Observatory, Columbia University, Palisades, New York, USA, [4]Department of Marine Geology and Geophysics, School of Oceanography, University of Washington, Seattle, Washington, USA

Abstract Time-series measurements of diffuse exit-fluid temperature and velocity collected with a new, deep-sea camera, and temperature measurement system, the Diffuse Effluent Measurement System (DEMS), were examined from a fracture network within the ASHES hydrothermal field located in the caldera of Axial Seamount, Juan de Fuca Ridge. The DEMS was installed using the HOV *Alvin* above a fracture near the Phoenix vent. The system collected 20 s of 20 Hz video imagery and 24 s of 1 Hz temperature measurements each hour between 22 July and 2 August 2014. Fluid velocities were calculated using the Diffuse Fluid Velocimetry (DFV) technique. Over the ~12 day deployment, median upwelling rates and mean fluid temperature anomalies ranged from 0.5 to 6 cm/s and 0°C to ~6.5°C above ambient, yielding a heat flux of 0.29 ± 0.22 MW m^{-2} and heat output of 3.1 ± 2.5 kW. Using a photo mosaic to measure fracture dimensions, the total diffuse heat output from cracks across ASHES field is estimated to be 2.05 ± 1.95 MW. Variability in temperatures and velocities are strongest at semidiurnal periods and show significant coherence with tidal height variations. These data indicate that periodic variability near Phoenix vent is modulated both by tidally controlled bottom currents and seafloor pressure, with seafloor pressures being the dominant influence. These results emphasize the importance of local permeability on diffuse hydrothermal venting at mid-ocean ridges and the need to better quantify heat flux associated with young oceanic crust.

1. Introduction

Measurements of hydrothermal exit-fluid temperatures and flow rates inform estimates of the heat and mass fluxes from deep-sea hydrothermal vents [e.g., *Germanovich et al.*, 2015; *Mittelstaedt et al.*, 2012; *Pruis and Johnson*, 2004; *Rona and Trivett*, 1992; *Schultz et al.*, 1992, 1996]. Quantifying these values, and how they change over time, provides key constraints on the hydrological architecture of hydrothermal systems, the evolution of associated ecosystems, long-term variations in ocean chemistry, and the thermal, physical, and chemical evolution of the oceanic crust [*Canales et al.*, 2006; *Cherkaoui et al.*, 2003; *Elderfield and Schultz*, 1996; *Escartin et al.*, 1997; *Lutz et al.*, 2008; *Nees et al.*, 2008]. In addition, detailed time-series measurements of these systems can constrain physical parameters associated with hydrothermal environments [e.g., *Barreyre et al.*, 2014a; *Barreyre and Sohn*, 2016; *Dziak et al.*, 2003; *Fornari et al.*, 1998; *Fujioka et al.*, 1997; *Little et al.*, 1988; *Scheirer et al.*, 2006; *Von Damm and Lilley*, 2004].

In general, the integrated heat and volume fluxes of a hydrothermal vent field are the sum of the inputs from diffuse, low temperature (predominantly <100°C) and focused, high temperature (predominantly >300°C) vents [e.g., *Bemis et al.*, 2012; *Di Iorio et al.*, 2012]. The relative magnitude of diffuse versus focused venting is likely related to the shallow crustal permeability structure and the geometry of heat sources driving flow [e.g., *Fornari et al.*, 2004; *Lowell et al.*, 2012, 2015], which varies between vents and between vent fields [e.g., *Mittelstaedt et al.*, 2012; *Ramondenc et al.*, 2006]. Thus, quantifying both diffuse and focused fluxes is necessary to yield a complete (i.e., global) estimate of hydrothermal heat flux associated with creation of oceanic crust at spreading ridges. To date only a few field experiments have measured both temperature and flow rates to calculate diffuse vent fluxes [*Barreyre et al.*, 2012; *Mittelstaedt et al.*, 2012 and

references therein]. Measurements that do exist are commonly based on repeated, short time duration "spot" measurements that are then used to estimate vent fluxes over a wide spatial area. These types of measurements yield a useful snapshot of a hydrothermal system's heat flux [e.g., *Barreyre et al.*, 2012; *Ginster et al.*, 1994; *Mittelstaedt et al.*, 2012]. "Spot" measurements do not, however, account for temporal variability in flow rates and temperatures. Understanding the variability of diffuse fluxes requires time-series measurements collected over numerous tidal cycles at specific vents. In studies where time-series measurements of diffuse venting have been made, observations suggest periodic, episodic, and random variability [*Pruis and Johnson*, 2004; *Schultz et al.*, 1992, 1996]. Studies documenting periodic or episodic variability may inform estimates of the parameters controlling fluid circulation, such as crustal permeability [e.g., *Barreyre et al.*, 2014a; *Crone et al.*, 2010]; however, few estimates have yet been attempted with diffuse flow data [e.g., *Prius and Johnson*, 2004].

To constrain parameters such as crustal permeability from time-series data, it is essential to first determine the primary processes driving periodic or episodic variations of hydrothermal venting. This can be difficult when multiple sources produce similar variability. For example, spectral analyses of focused and diffuse venting at several different vent fields show that periodic flow rate variations commonly have peaks in power spectral density (PSD) at diurnal or semidiurnal tidal frequencies [e.g., *Scheirer et al.*, 2006; *Sohn*, 2007; *Tivey et al.*, 2002]. Diurnal and semidiurnal variability in diffuse venting have previously been attributed to tidal changes in pressure at the seafloor [e.g., *Barreyre et al.*, 2014b; *Pruis and Johnson*, 2004], tidally modulated bottom currents [e.g., *Tivey et al.*, 2002; *Scheirer et al.*, 2006], or both depending upon local tidal response [*Sohn*, 2007]. It remains unclear to what extent these two sources modulate the periodic variability of diffuse venting.

In this study, we present and analyze data from a newly developed deep-sea camera platform, the Diffuse Effluent Measurement System (DEMS), designed to perform noninvasive, time-series measurements of diffuse effluent temperatures and flow rates. The DEMS was deployed for ~12 days in the ASHES (Axial Seamount Hydrothermal Emissions Study) hydrothermal vent field [*Malahoff et al.*, 1984], where it collected >250 h of exit-fluid temperature and velocity measurements. Data from the DEMS demonstrate that it is an effective system for monitoring diffuse venting. Together, these data allow calculation of the local heat flux and an estimation of the diffuse heat flux from cracks within the ASHES vent field. They also allow quantification of the variability in both temperature and velocity measurements and determination of the most probable source of the variability. Results show periodic variations in both effluent temperature and upwelling velocities. Analyses of these variations indicate that both bottom currents and tidally induced seafloor pressure variations may control the measured variability, but that pressure variations likely dominate.

1.1. The ASHES Hydrothermal Field and the Phoenix Vent

The ASHES hydrothermal field is located in the southwest corner of Axial Seamount's caldera [*Malahoff et al.*, 1984], which is located on the crest of the intermediate-spreading Juan de Fuca Ridge (Figure 1). The majority of vents in the ASHES field are situated within a ~60 m wide, ~1–2 m deep depression (Figure 2) located ~100 m east of the caldera's western wall. The field hosts few (<10) chimneys (<5 m tall), each with multiple high-temperature (~200–350°C), focused orifices emitting hydrothermal fluids [*Butterfield et al.*, 1990, 2004; *Kelley et al.*, 2014]. The field also hosts an isolated anhydrite chimney venting high temperature, gas-rich fluids [i.e., Virgin Mound, *Butterfield et al.*, 1990]. Surrounding the high-temperature vents are networks of thin cracks that are generally <10 cm wide and host active outflow. Many of the cracks emitting low temperature diffuse fluids are lined by white bacterial mats intermixed with small tubeworms and clams [*Butterfield et al.*, 2004; *Kelley et al.*, 2014]. The field also hosts patches, a few meters across, of bacterial mats with variable concentrations of vent endemic macrofauna.

The Phoenix vent is a ~2 m tall chimney located along the southern boundary of the ASHES field (Figure 2). The structure hosts ~2 separate orifices that emit high-temperature effluent with measured temperatures of ~300°C. In addition to focused sites of flow, the outer walls are awash in lower temperature variable mixtures of hydrothermal and seawater fluids, which are diffusely venting and support dense macrofaunal communities. Approximately 10 m southeast of the Phoenix chimney, on a flat, sheet-lobate lava flow, steady diffuse effluent exits from several parallel, linear, narrow (~3 cm wide) cracks coated with white bacterial mats (Figure 3). The proximity of these narrow cracks in the volcanic carapace to the high-temperature Phoenix vent and the nearly flat bathymetry provided an ideal location for deployment of the DEMS system. In addition to the DEMS, the VentCam [*Crone et al.*, 2014], a camera system designed to capture high-resolution, time-lapse imagery used to calculate high-temperature vent fluxes in a nonintrusive manner was
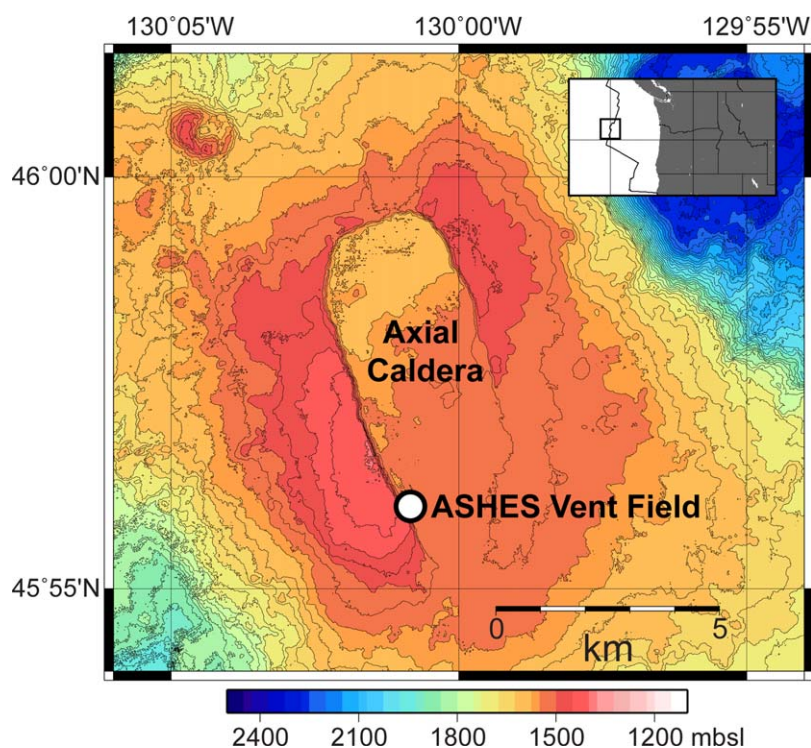
Figure 1. The ASHES vent field (white dot) is located in the southwest corner of the Axial caldera along the Juan de Fuca Ridge (inset, black line) [*Bird*, 2003] approximately 400 km west of the Oregon coast. Bathymetric data are from *Chadwick et al.* [2015].

contemporaneously deployed at the Phoenix Vent during the experiment. The objective of the coincident deployment of these two systems was to conduct synchronized measurements of flow rates of proximal diffuse and focused vents. Results from the VentCam deployment will be published elsewhere.
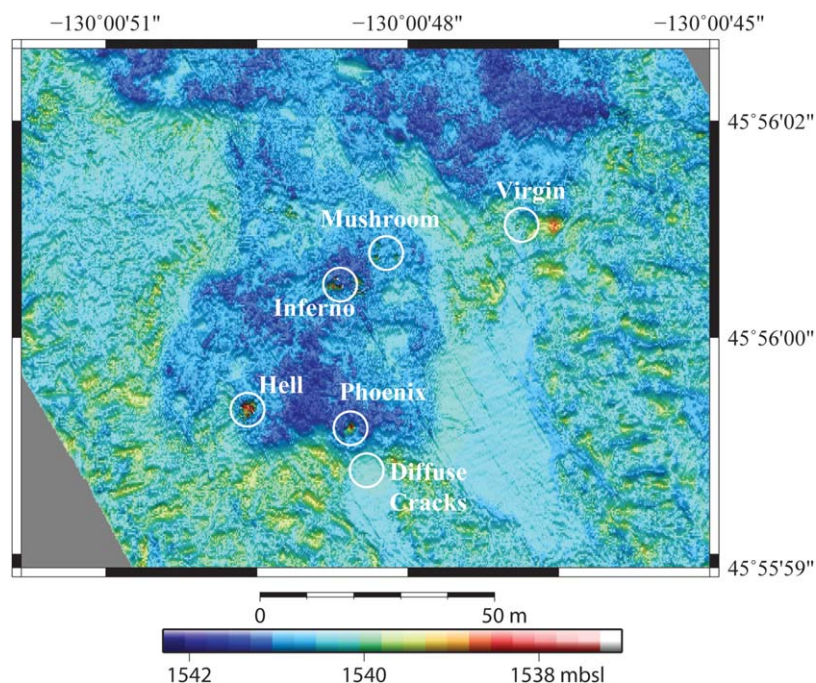

Figure 2. The DEMS camera was deployed above a linear, narrow crack located ~10 m southeast of the high temperature Phoenix vent (Diffuse Cracks). The Phoenix vent is located along the southern edge of a small depression that hosts the majority of the high-temperature vents (white circles) of the ASHES vent field. The near-bottom multibeam bathymetry map (gridded at 0.25 m) was acquired at an altitude of 10 m above the seafloor by the autonomous underwater vehicle (AUV) *Sentry* using the RESON 7125 Seabat sonar.
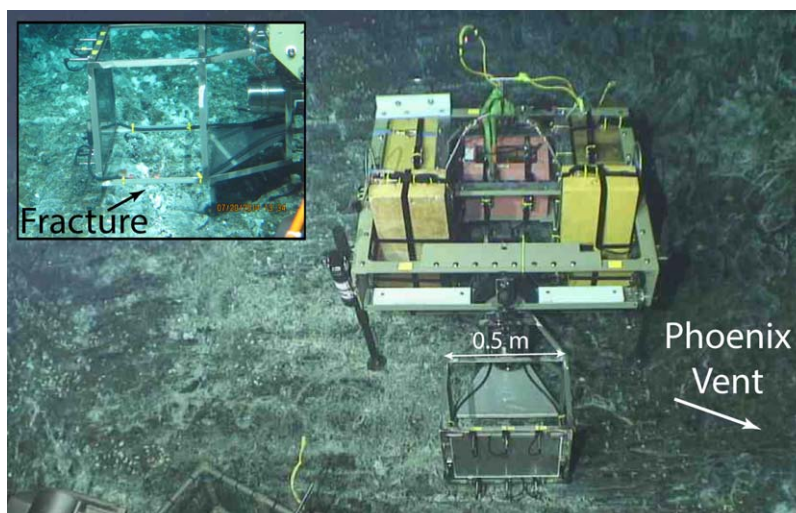
Figure 3. The DEMS was deployed at a depth of 1541 m above a linear narrow crack exhibiting active, steady diffuse venting. The aluminum frame supporting the camera housing and the background board was placed where diffuse flow was observed to pass in front of the image board, within view of the camera and over the thermistor tips (inset).

2. The Diffuse Effluent Measurement System

The DEMS is a new, deep-sea camera system that captures digital imagery and measures temperatures of upwelling, diffuse hydrothermal effluent passing between a camera and a rigid image board with a back-illuminated random-dot pattern printed on its camera-facing side (Figure 3). The camera captures a series of images of the illuminated background, which appear distorted by differences in the index of refraction between ambient seawater and the diffuse effluent. These moving imagery data are ideal for post processing using Diffuse Flow Velocimetry (DFV) [*Mittelstaedt et al.*, 2010], a noninvasive, two-step cross-correlation method of image analysis to calculate fluid velocities (section 3.1). Coregistered with the imagery, the system measures effluent temperature using six calibrated thermistors located along the base and top of the image board (Figure 4). The combination of coregistered fluid velocities and temperatures allows accurate, minimally invasive time-series estimates of local, diffuse hydrothermal heat flux.
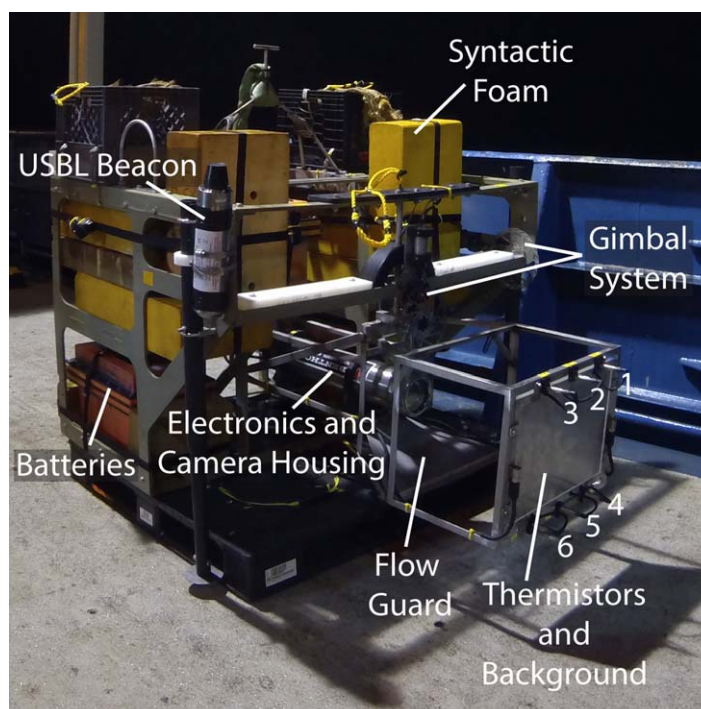

Figure 4. The DEMS consists of two frames. The primary, outer frame is made of Extran fiberglass and holds three lead-acid batteries, the electronic junction box (not visible), syntactic foam, and the secondary frame. The secondary, smaller aluminum frame holds the image background frame, thermistors (as numbered), and the titanium electronics and camera housing. The secondary frame is attached to the primary frame through a gimbal system to allow the camera to be level despite uneven terrain at a deployment location.

2.1. System Details
2.1.1. Gimbaled Camera Frame
Depending on the local seafloor geology at a vent, the DEMS may encounter sloped or rough terrain and the local direction of
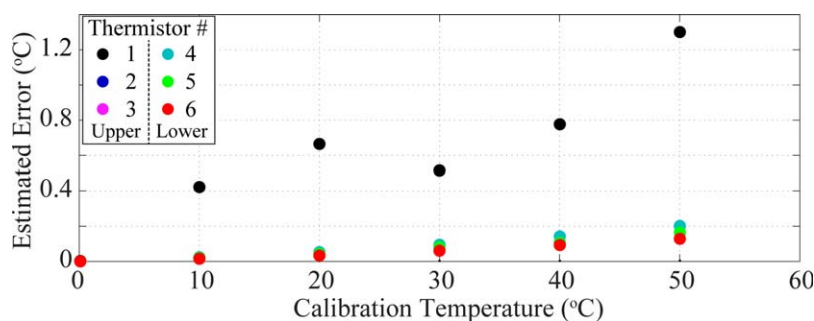
Figure 5. Prior to deployment, thermistor calibration was performed at 10°C intervals between 0°C and 50°C. The estimated accuracy of each thermistor was estimated as the standard deviation of the measured temperatures at each calibration temperature (colors). Thermistor 1 (black circle) exhibited relatively large errors during this calibration. Values for thermistors 2 and 3 are not visible due to overlap of the data points.

the gravity vector (vertical) may not correspond to "up" in the camera image frame. To ensure that captured image frames are aligned with the local gravity vector and that the frame does not block upwelling flow, the DEMS titanium housing (containing the system computer, electronics, and camera) and the Electroluminescent Speckle Image Emitter panel (ELSIE—section 2.1.3) are mounted 0.5 m apart on a secondary frame that is separate from the main structural frame of the system (Figure 4). The secondary frame is mounted within the larger, main frame by a gimbal system with solenoid brakes. Once installed on the seafloor, the solenoid brakes are released by a magnetic switch and the secondary frame is allowed to come to rest horizontally; the brakes are then reengaged to lock the frame in place.

2.1.2. Thermistors

The DEMS registers in situ fluid temperatures using six SeaBird© Model BR14KA802L thermistors (http://www.cdiweb.com/datasheets/ge_thermometrics/br111416.pdf; Figure 4) mounted inside thin (~1 mm) metal tips. The thermistors are affixed to the ELSIE panel and protrude ~3.5 cm from behind the board into the flow. Each thermistor tip is at the same distance from the surface of the ELSIE. To measure temperatures as fluid enters and exits the camera's field of view, three thermistors are placed along the bottom and three along the top of the image board. Due to their small cross-sectional area, the thermistors have a very small effect on fluid flow patterns; for the purposes of our calculations we have assumed that there is no impact on flow rates. Each thermistor was calibrated every 10°C between 0°C and 50°C by plunging the thermistor into a water bath of known temperature followed by an ice bath between each measurement. The response time of each thermistor was <1 s with an accuracy better than ±0.1°C for temperatures <40°C, except for thermistor 1. The calibration results for thermistor 1 indicated a standard deviation in voltage levels corresponding to as much as ±1.4°C at 50°C (Figure 5); this variability is considered unacceptable and measurements from thermistor 1 were excluded. In addition, thermistors 2 and 4 suffered failures during deployment, possibly due to pressure or physical damage. Time-averaged (over each 24 s measurement period) temperatures measured by thermistors 3, 5, and 6 prior to deployment were 16.43°C, 16.60°C, and 16.77°C, respectively. This discrepancy may indicate thermistor offsets of 0.18°C to 0.35°C, but it is difficult to determine if the offset is caused by measurement error or environmental variability, because the DEMS was sitting on deck and exposed at this time. During video acquisition, the DEMS recorded thermistor measurements at a rate of 1 Hz. No corrections or shifts in the thermistor data were made to remedy the observed differences because the source of the offsets could not be verified. It is possible that the offsets introduce a small shift in the temperatures, but they do not appear to interfere with variability of the measurements during the monitoring experiment, hence the derived flux values and our spectral analyses will not be significantly impacted.

2.1.3. Imaging System

All electronics for the DEMS system are contained within a 6000 m rated, titanium pressure vessel mounted on the secondary, gimballed frame at a camera-background distance of 0.5 m. The DEMS captures images of the ELSIE at a resolution of 1380 × 1024 pixels using a Prosilica GE1380 machine vision camera fitted with a 12.5 mm Fujinon lens. The end of the housing facing the image background board contains a flat-port optical glass element through which the images are acquired. The camera focus is adjusted prior to deployment using a reference pattern and then fixed for the duration of the deployment, resulting in good
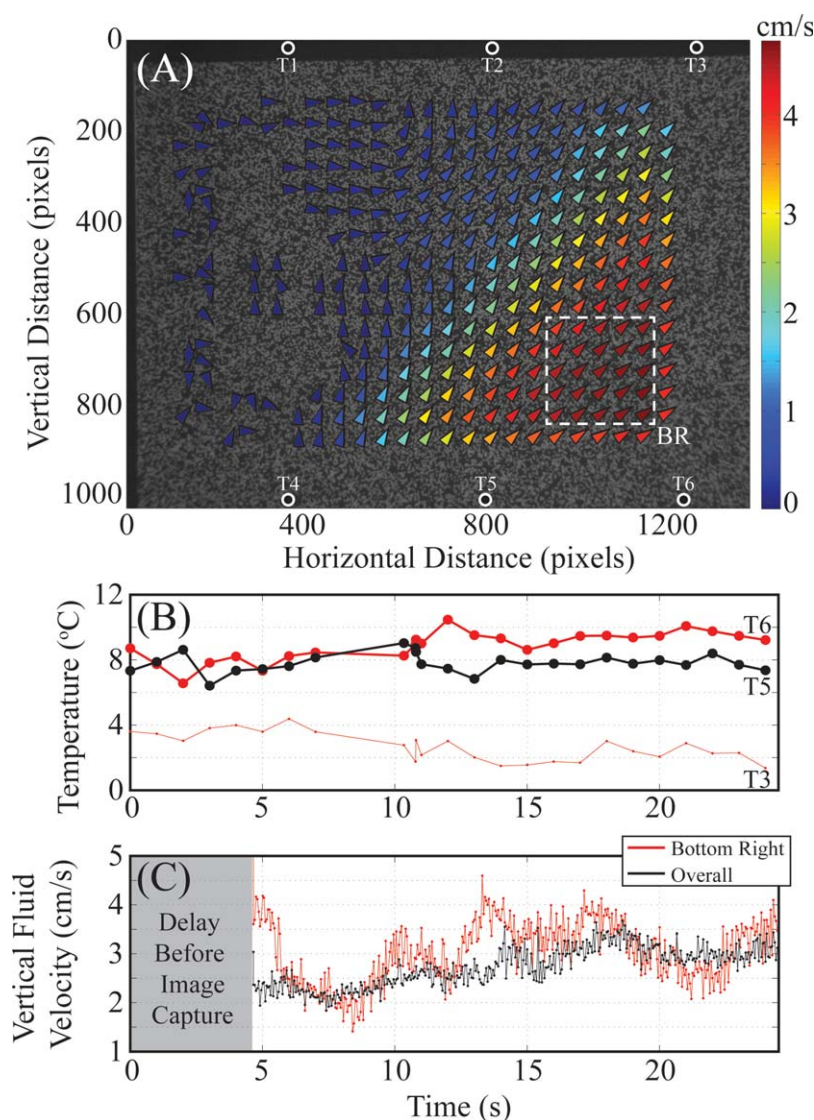
Figure 6. (a) Time-averaged (over 20 s) velocity vectors at each location where DFV was used to calculate fluid flow rates (colors) shown on an image of the background board. Thermistors are located slightly outside of the image frame, but their locations are shown (white circles, as labeled). (b) Temperatures measured by thermistors 3 (thin, red line), 5 (thick, black line), and 6 (thick, red line) during a 24 s period at 1500 h on 1 August 2015. (c) Median velocities at each DFV calculation from the entire image frame (black) and the bottom right (white-dashed line in Figure 6a) of the image frame (red). During this measurement period, flow was concentrated on the right side of the frame. Imagery collection began ∼4 s after temperature measurements began.

image focus throughout the region of interest (Figure 6a). The ELSIE is a background board backlit by four low-power, electroluminescent panels potted within a clear, acrylic resin behind the random dot pattern (measuring 40 cm × 30 cm). To control image capture, the DEMS uses a picoITX form-factor computer powered by a 1.6 Ghz Intel[TM] Atom processor with 2 Gb of RAM. The picoITX form-factor was chosen to minimize size and power usage. Power for these systems is provided by three MISO (Multidisciplinary Instrumentation in Support of Oceanography; http://www.whoi.edu/main/instruments/miso) 40 amp/h deep-sea Pb-acid, oil-compensated batteries (Figure 4), which are estimated to provide sufficient power for >1 month of measurements.

2.2. Deployment at the Phoenix Vent, ASHES Hydrothermal Field
Deployment of the DEMS in the ASHES field occurred on 22 July 2014. The system was wireline deployed using the hydrographic wire on the R/V *Atlantis* to a height of ∼5 m above the seafloor and then released by acoustic signal and allowed to free-fall the remaining distance. The human-occupied vehicle (HOV) *Alvin*

then maneuvered the DEMS from the wireline deployment location to a linear crack ~10 m southeast of the Phoenix vent (Figure 3). Using *Alvin*'s manipulators, the DEMS was moved into place with the ELSIE directly in line with and above the target crack in the lava surface. The solenoid brakes on the gimbaled secondary frame were then released until the image board was vertical and the camera level. The brakes were then reengaged. After installation of the system, diffuse flow was observed to pass through the camera's field of view and over all six thermistors (Figure 3). During the deployment, imagery and temperatures were recorded once per hour for 20 s and 24 s, respectively. On 2 August, a floatation package was deployed to the seafloor and attached to the system by *Alvin*. The floatation brought the DEMS to the sea-surface and it was recovered by the crew of R/V *Atlantis*. The deployment of ~12 days resulted in >250 hourly measurements of velocities and temperatures of diffuse flow.

3. Methods

3.1. Diffuse Flow Velocimetry

Details of the DFV method are presented in *Mittelstaedt et al.* [2010], but a brief summary is presented here. The DEMS captures a series of video images of a motionless, random dot pattern as viewed through the lens of a moving refraction index anomaly (e.g., a hot upwelling fluid passing through background seawater). When viewed in two sequential images, the background dot pattern appears to deform (e.g., the dots appear to move) due to movement of the refraction index anomaly, which changes the pattern of apparent distortion in the image. This change in the apparent distortion is a function of the displacement of the index of refraction anomaly and would not be visible in the case of zero motion. The direction any given pixel appears to move due to this distortion depends upon index of refraction gradients and, thus, can occur in any direction, not only in the direction of motion. However, over time the movement of the refraction index anomaly will cause the apparent distortion to move across the image at the rate of fluid flow; over short-time periods (<~1 s) the pattern of deformation remains unchanged and can be tracked. The two-step DFV calculation first determines the apparent deformation between sequential background images and then tracks movement of the apparent deformation pattern between these deformation calculations to estimate fluid velocities.

In the first step of the DFV method, the deformation field is determined using a multilevel Particle Image Velocimetry (PIV) algorithm [e.g., *Westerweel*, 1997; *Willert and Gharib*, 1991]. Particle Image Velocimetry divides images into a grid of overlapping windows. A succession of window sizes is utilized from 32×32 pixels to 8×8 pixels, each with an overlap of 50%. Using Fourier convolution, intensities of the pixels within each window are cross-correlated with intensities in the subsequent image. The location of the maximum correlation corresponds to the highest probability displacement of the window caused by movement of the refraction index anomaly. Repeating this calculation across all pixel windows in an image produces an instantaneous 2-D vector field of the apparent background deformation due to movement of the index of refraction anomaly between two images.

The second step of a DFV calculation tracks the pattern of apparent background deformation vectors as they move slightly with the fluid between PIV calculations. Similar to the PIV calculation, two subsequent deformation vector fields are divided into overlapping windows of vectors. A single window size of 8×8 vectors was used with a 50% overlap. For each window, the X and Y components of each apparent deformation vector are cross-correlated to determine the highest likelihood shift of the vector window, thus giving the shift associated with fluid motion in the time between two calculations (e.g., approximated fluid velocity). The precision of the location of the correlation minimum is improved from ± 0.5 times the distance between vector locations to $\sim \pm 0.1$ times the intervector distance with an analytical 3-point Gaussian fit in both coordinate directions [*Willert and Gharib*, 1991]. This calculation is performed on all the vector windows to yield the instantaneous, 2-D velocity field.

The location of the maximum correlation gives the highest probability displacement of the deformation field in the window, but outliers can occur due to poor image quality, little, or no fluid movement, and/or undetectable deformation (due to very small, very large, or nonexistent density variations). Two methods are used to limit false correlations. First, the velocity is considered valid only if the curvature of the correlation peak in the immediate neighborhood of the correlation maximum is greater than an empirically determined critical value of 1×10^{-5}. Second, a window shift is considered invalid if it falls on the boundary of

the correlation matrix. If a given shift fails these tests, it is assumed to be erroneous and the velocity in that location is set to 0. Finally, the calculated velocities are smoothed by a 3×3 median filter.

Particulate matter in the water is another potential source of error during DFV processing. During deployment of the DEMS, low densities of particulate matter were observed within the upwelling diffuse effluent, but higher concentrations were present in the laterally flowing bottom currents. Higher concentrations of particles can decrease the quality of DFV calculations, but this is not always the case. In general, floating particles yield one of two effects: (1) the correlation peak near the particle is poor and the value is thrown out as described above, or (2) the calculation treats the particle motion as apparent deformation and will follow this "deformation" across two calculations yielding the velocity of the particle, which should be similar to the fluid velocity. Each individual particle only interferes with a single velocity vector calculation, limiting their impact on flow calculations when the density is low. Yet, even in the case where numerous particles are present in an image, the velocity field will still represent the motion of the fluids and/or vectors will be removed where poor correlations occur. Thus, particulate manner is likely to have only a small impact on DFV calculations.

3.2. Data Records
Data records from the DEMS were corrected for clock drift and trimmed to the period of interest (i.e., the time period during which the system was deployed over the diffuse effluent issuing from the crack in the lava surface). The internal clock on the DEMS computer was synchronized to Coordinated Universal Time (UTC) before and after deployment to the seafloor. Total clock drift over the 12 day deployment was ∼8 s; a correction was applied to all timing data assuming a linear drift. Trimming of the data record was performed because the DEMS measurements were initialized while the system was on deck, prior to deployment, and continued until the system was shut down once the system was recovered.

3.3. Time-Series Analysis
Previous studies calculate the spectral content of uniformly spaced time-series temperature and/or velocity measurements by applying Fourier methods [e.g., *Barreyre et al.*, 2014a; *Scheirer et al.*, 2006; *Schultz et al.*, 1992; *Tivey et al.*, 2002]. However, gaps in our velocity measurements (section 4.2) make using these techniques difficult. To avoid the problem of data gaps, the normalized spectral power of our velocity time-series was calculated by applying a per-point method, the Lomb-Scargle Periodogram [*Lomb*, 1976; *Scargle*, 1982]. The Lomb-Scargle method is equivalent to estimating the harmonic content of the data set at a given frequency through a least-squares fit to $h(t) = A\cos(wt) + B\sin(wt)$, where h is the power, w is angular frequency, t is time, and A and B are constants [*Press et al.*, 2002]. Although the DEMS temperature measurements are uniformly spaced, the temperature spectra were estimated using the Lomb-Scargle Periodogram to facilitate comparison with the velocity analysis.

In addition to the examination of spectral peaks, the coherence and phase lags between temperature measurements from each thermistor were investigated, as well as between the temperature measurements and modeled tidal heights [*Matsumoto et al.*, 2000]. Although offsets in absolute temperature of up to 0.35°C are present before deployment of the DEMS, we are interested in variability of the measured values, and the variability is similar between thermistors and does not appear to be erroneous. The coherence between velocity measurements and other time-series data were not calculated because of uneven data spacing. Similar to previous studies [e.g., *Barreyre et al.*, 2014b; *Tivey et al.*, 2002], coherence and phase lag are calculated using multitaper [*Thompson*, 1982] and adaptively weighted cross-spectral methods [*Percival and Walden*, 1993]. Following *Barreyre et al.*, [2014a], errors in phase shifts are estimated by jackknifing the independent phase estimates obtained for each of the orthogonal tapers. These methods were applied to the time series of hourly, median temperatures and coincident tidal pressure estimates.

4. Diffuse Effluent Temperatures, Velocities, and Heat Flux

4.1. Temperature Measurements
The DEMS measured fluid temperatures at a rate of 1 Hz for a period of 24 s each hour, coincident with image capture during the deployment period. Of the six thermistors on the DEMS, we only use temperatures from thermistors 3, 5, and 6. As shown in Figure 6a, thermistor 6 is located just below the bottom right portion of the image frame with thermistor 3 located ∼35 cm above thermistor 6. Thermistor 5 is located
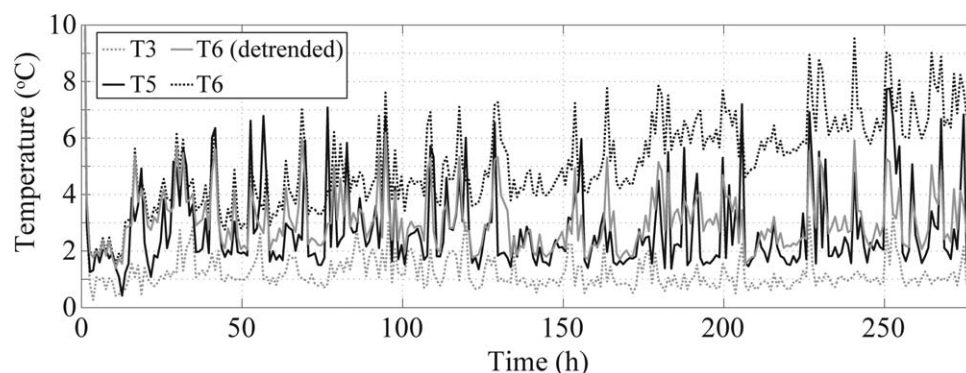
Figure 7. Temperature measurements acquired by thermistors 3, 5, and 6 (as noted). Temperatures measured by thermistor 6 steadily increased throughout the measurement period, and are presented as measured (solid gray line) and detrended (dashed black line). To calculate the detrended record, we remove a linear trend of 0.015°C/h determined by a least squares linear fit to the thermistor 6 record (6dt).

∼12.9 cm to the left (horizontally) of thermistor 6. For an ideal flow that rises vertically due to buoyancy, thermistors 3 and 6 would measure the change in temperature across the image frame; in general, the flow is not perfectly vertical. Hence, temperatures registered at a vertically oriented pair of thermistors do not always correspond to temperatures in the same diffuse upwelling. Thus, data from thermistors 5 and 6 were used to represent spatially "lower" temperatures and data from thermistor 3 as representing "upper" temperatures.

Throughout the hourly 24 s recording period, temperature measurements for individual thermistors and between thermistors remained approximately steady, but, occasionally, there were trends or periods of high-frequency variability (Figure 6). For example, temperature measurements from thermistor 3, 5, and 6 on 1 August at 1500 h show abrupt changes by as much as 2°C on timescales of ∼1–2 s (Figure 6). During the same 24 s measurement period, temperatures measured by thermistor 3 steadily decreased from ∼4°C to ∼2°C. Between thermistors, differences in temperature measurements are primarily controlled by the vertical thermal gradient close to the seafloor; thermistor 3 often measured temperatures up to several degrees lower than thermistors 5 and 6. During periods of low flow, however, the vertical temperature gradient across the ELSIE was ∼1°C.

Median temperature values (across each 24 s measurement period) vary periodically during the ∼12 day DEMS deployment, but do not vary episodically as observed in some studies [e.g., *Sohn* 2007]. However, episodic variations may occur at periods longer than the DEMS deployment. Values from all three thermistors vary similarly over periods of hours (Figure 7). Thermistors 3 and 5 maintain steady minimum values (i.e., no consistent trend), but measurements from thermistor 6 increase throughout the deployment. It is possible that diffuse effluent temperatures increased around thermistor 6 causing this warming trend, but the trend may also be due to instrument drift, perhaps caused by heating of the thermistor housing. To account for this possible drift, a linear fit of 0.015°C/h was removed from thermistor 6 values, as determined by a least squares fit.

The following analysis includes values from thermistor 6 and values from the detrended thermistor 6, hereafter referred to as 6dt, but primarily focuses on the detrended values. Temperatures recorded by thermistors 5 and 6dt have similar ranges and consistent variability (Figure 7). Thermistor 3 temperatures are ∼1°C lower than those measured by thermistors 5 and 6dt, likely due to cooling of diffuse fluids as they rise to the height of thermistor 3. Smaller temperature peaks measured by thermistors 5, 6, and 6dt do not always register on thermistor 3 (e.g., Figure 7 ∼48 h after deployment). This suggests that some warmer fluids do not traverse the image board before being diverted by bottom currents or cooling to ambient temperatures. Overall, the mean and standard deviation of temperatures for thermistors 3, 5, 6, and 6dt were 1.2 ± 0.5°C, 2.8 ± 1.5°C, 5.2 ± 1.6°C, and 3.1 ± 1.0°C, respectively.

4.2. Velocity Measurements
For each measurement period, the DFV method was used to calculate a grid of 24 × 16 velocity vectors over each set of ∼400 images (20 s at 20 Hz). Despite rapid, small-scale spatial variations, a preferred flow
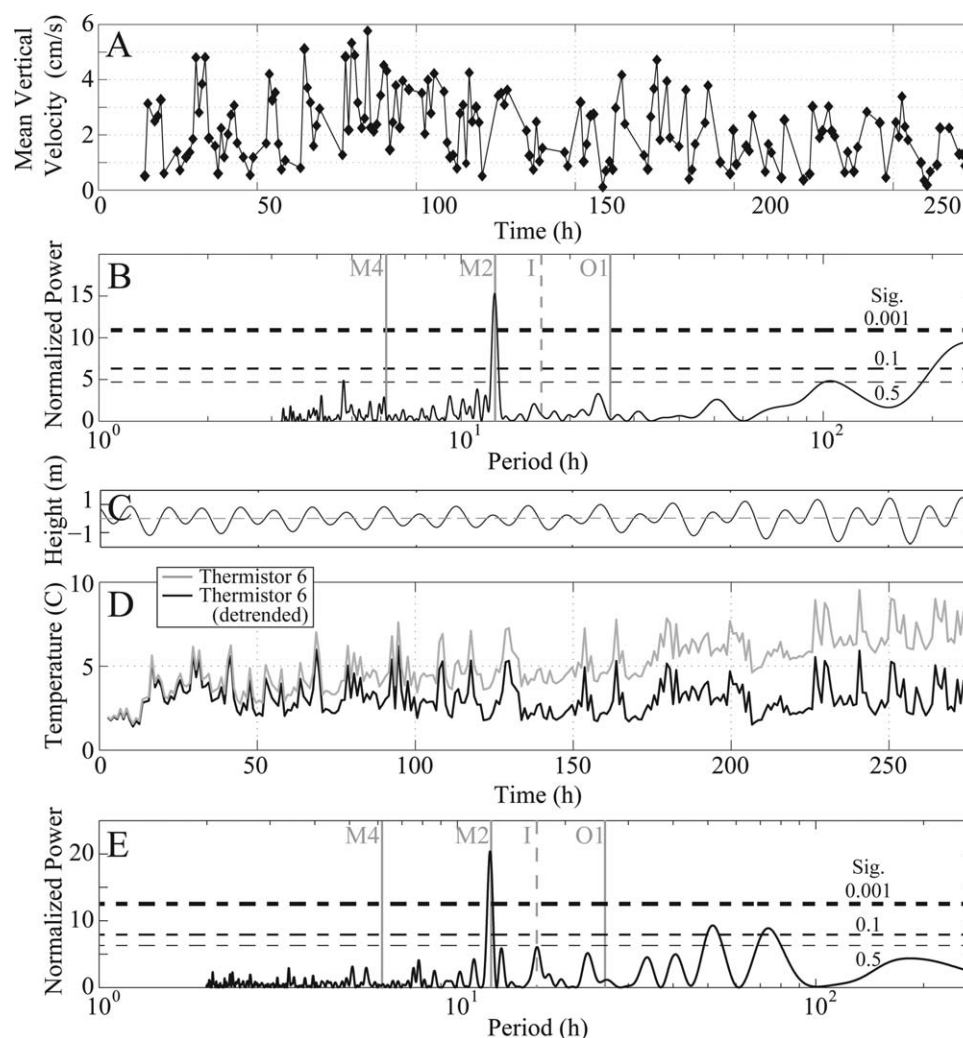
Figure 8. (a) Vertical velocities of the diffuse effluent rising into the DEMS image frame vary periodically with (b) a peak in normalized power at the M2 semidiurnal period (12.4 h). Strong currents during the largest (c) modeled tidal height variations resulted in gaps in the velocity measurements. Similar to the velocities, (d) temperatures of diffuse effluent show (e) periodic variability with a large peak in normalized spectral power at the M2 semidiurnal period. The temperatures from thermistor 6dt also have peaks at ∼2 and ∼3 day periods. A peak at the 3 day period is seen in thermistor 3, but not in thermistor 5 (supporting information Figures S4 and S5).

direction is observed during each measurement period where flow is present. To assess the average flow rate and direction for each 20 s measurement window, the median flow rate was calculated at each vector location by separately considering the horizontal and vertical vector components (vectors removed by DFV error corrections are ignored). Repeating this calculation at each vector location yields a single grid of median flow rates for one measurement period (Figure 6a). Velocity results show that diffuse effluent preferentially rises in the bottom right of the image board, suggesting that this part of the crack may have a higher average flux. However, the location of greatest average flow varies across the entire base of the image frame, depending upon the prevailing direction of bottom currents.

Shifts in the horizontal component of diffuse flow velocities through time indicate a periodic change in the direction of bottom currents. At some times, bottom currents diverted the rising diffuse effluent out of the camera view preventing DFV calculations and, therefore, velocities are not available for these measurement periods. Overall, strong currents cause a loss of ∼40% of the potential velocity data (supporting information Figure S1). Yet, data loss is not consistent across the deployment and uninterrupted measurements exist for periods up to 34 h, primarily during lower magnitude tides early in the deployment (Figure 8c). Temperature data are not interrupted during periods of strong currents, but the measured temperatures at these
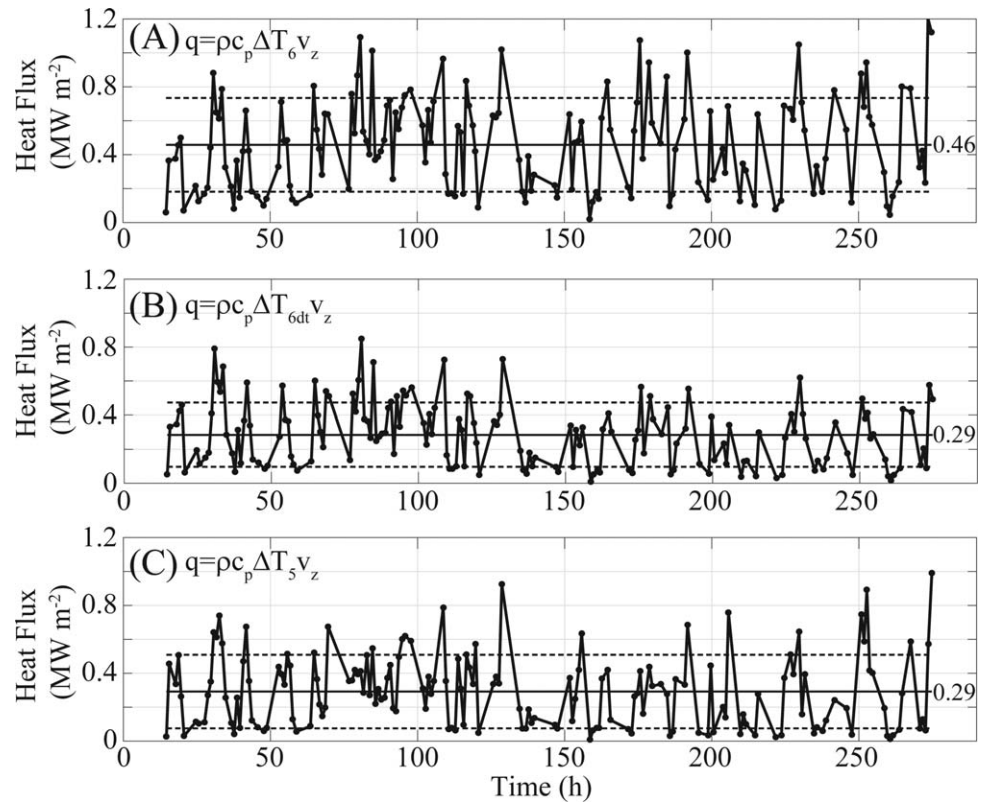
Figure 9. Heat flux density is a function of fluid temperature and upwelling velocity. The heat flux density of the narrow crack beneath the DEMS was estimated for each of (top to bottom) thermistors 6, 6dt, and 5 to be 0.46 ± 0.28 MW m^{-2}, 0.29 ± 0.19 MW m^{-2}, and 0.29 ± 0.22 MW m^{-2}, respectively. Mean values are denoted by a solid line with the standard deviation denoted by dashed lines.

times may not reflect temperatures of diffuse effluent. The loss of velocity measurements in periods of strong currents may introduce a bias into our frequency analysis. This is discussed in section 5.1.

To investigate changes in upwelling velocity across several periods of image capture (i.e., over hours or days), the grid of median velocities was averaged spatially. Measured total flow rates range from 1.7 to 8.7 cm s^{-1} with a vertical component between 0.1 and 5.8 cm s^{-1}. Similar to the temperature measurements, the calculated velocities vary periodically, but not episodically.

4.3. Diffuse Heat Flux

At each measurement period with an available velocity calculation, the diffuse heat flux of the thin crack beneath the DEMS was determined (Figure 9). The diffuse heat flux q was calculated using the spatially averaged velocity representative of that measurement period and the time-averaged temperature such that

$$q = \rho c_p v_z (T_n - T_{ambient}) \qquad (1)$$

where v_z is the vertical component of the velocity, ρ is the density of seawater (1030 kg m^{-3}), c_p is the heat capacity of seawater at constant pressure (4000 J kg^{-1} K^{-1}), $T_{ambient}$ is the temperature of ambient seawater at the Phoenix vent taken to be the mean of the minimum values during each measurement period from thermistor 3 (0.35°C), and T_n is the time-averaged temperature measured by thermistor n. To estimate a single diffuse heat flux density for the crack, the mean and standard deviation of the time series of heat fluxes calculated with equation (1) were used (Figure 9), which gives 0.29 ± 0.22 MW m^{-2} for thermistor 5, 0.29 ± 0.19 MW m^{-2} for 6dt, and 0.46 ± 0.28 MW m^{-2} for thermistor 6. By measuring the crack width (3 ± 0.5 cm) from *Alvin* video and determining the span of the image frame covered by velocity calculations (31.4 cm), a heat output from the narrow crack beneath the DEMS of 3.1 ± 2.5 kW was calculated for the duration of the deployment period.

Table 1. Period and Peak Significance at Maximum Power

Measurement	Period at Max Power (h)	Significance Number (Lower Indicates Higher Probability)
Thermistor 3	12.3	2.97×10^{-3}
Thermistor 5	12.34	1.75×10^{-4}
Thermistor 6	12.34	3.82×10^{-7}
Velocity BR	12.28	4.09×10^{-3}
Velocity all	12.38	3.76×10^{-5}
Modeled tides	12.42	0[a]

[a]To machine precision.

4.4. Integrated Diffuse Heat Output From Thin Cracks Across the ASHES Vent Field

To estimate the integrated heat output attributable to networks of narrow cracks across the entire ASHES field (which covers an area of $\sim$3600 m^2), the new heat flux measurements from the single thin crack were used in conjunction with measurements of narrow crack length and width digitized on a mosaic of high resolution ($\sim$1 mm per pixel) photographs [*Kelley et al.*, 2014] (supporting information Figure S2a). To estimate the heat output from these narrow cracks, heat flux based upon the DEMS measurements was multiplied by the estimated spatial area of all narrow cracks throughout the ASHES field. The lengths of thin cracks were manually digitized where there were visible bacterial mats, yielding a total length of 212.24 m (supporting information Figure S2). Crack widths measured at 50 locations distributed across the vent field yielded values between 0.6 cm and 9.2 cm, forming a Poisson distribution (supporting information Figure S3) with a Poisson parameter of $\lambda = 2.2$ cm. The mean of the Poisson distribution of narrow crack widths is given by the parameter λ and the standard deviation is $\sqrt{\lambda}$ (1.49 cm). Thus, narrow crack widths are estimated to be 2.2 ± 1.5 cm. This estimate is consistent with the $\sim$3 cm width of the fracture beneath the DEMS as measured from *Alvin* video, as well as previous estimates of crack widths ($<$5 cm) in the southeast portion of the ASHES field [*Pruis and Johnson*, 2004]. Using these values and the calculated diffuse heat flux, we estimate a diffuse heat output from thin cracks across the ASHES hydrothermal field of 2.05 ± 1.95 MW. This value is based upon the heat flux measured by the DEMS during our deployment period and the measurements of cracks across the *Kelley et al.* [2014] photomosaic captured in 2010. It is possible that the network of active fractures changed during this time period, but the overall crack pattern is useful for placing the DEMS measurements into a broader vent field context that can be compared to measurements at other locations.

4.5. Variability of Flow Rates and Fluid Temperatures

Measured temperatures and velocities of diffuse effluent vary periodically with greatest spectral power at the semidiurnal tidal period (M2) [*Matsumoto et al.*, 2000]; (Table 1 and Figure 8). No spectral peaks are observed at the M4 or inertial periods. Spectral peaks above the 90% confidence level do exist at approximately 2 and 3 day periods in temperatures measured by thermistor 6dt (Figure 6e) and at the 3 day period in temperatures measured by thermistor 3, but no other peaks are present in data from thermistor 5 (supporting information Figures S4 and S5). For comparison, modeled tidal heights have periodic variability at semidiurnal (M2, N2, and S2), as well as diurnal (O1 and K1) periods.

Coherence between individual thermistor records can inform the spatial differences in fluid temperatures across the DEMS field of view. Coherence values are high between thermistor records (0.8–0.85) at the $\sim$12 h period (Table 2 and Figure 10), demonstrating covariance at the semidiurnal period of temperatures measured by all three thermistors that functioned during the experiment. At periods longer than $\sim$20 h, coherence is greatest between thermistors 3 and 5 and smallest between thermistors 3 and 6dt. For periods between $\sim$8 h and $\sim$15 h, coherence is highest between thermistors 5 and 6dt and relatively low between 5 or 6dt and 3. Greater coherence values between the thermistors located along the base of the image board (5 and 6dt) suggests that flow rate changes at these periods may fail to reach the position of thermistor 3. At shorter periods, the coherence values are much more variable; they drop significantly between thermistor 3 and the other thermistors, but remain relatively high between thermistors 5 and 6dt.

To better constrain how changes in tidal pressure modulate flow variability, the coherence and phase shift between the measured temperatures and modeled tidal heights [*Matsumoto et al.*, 2000]

Table 2. Coherence and Phase Shift at M2 Period

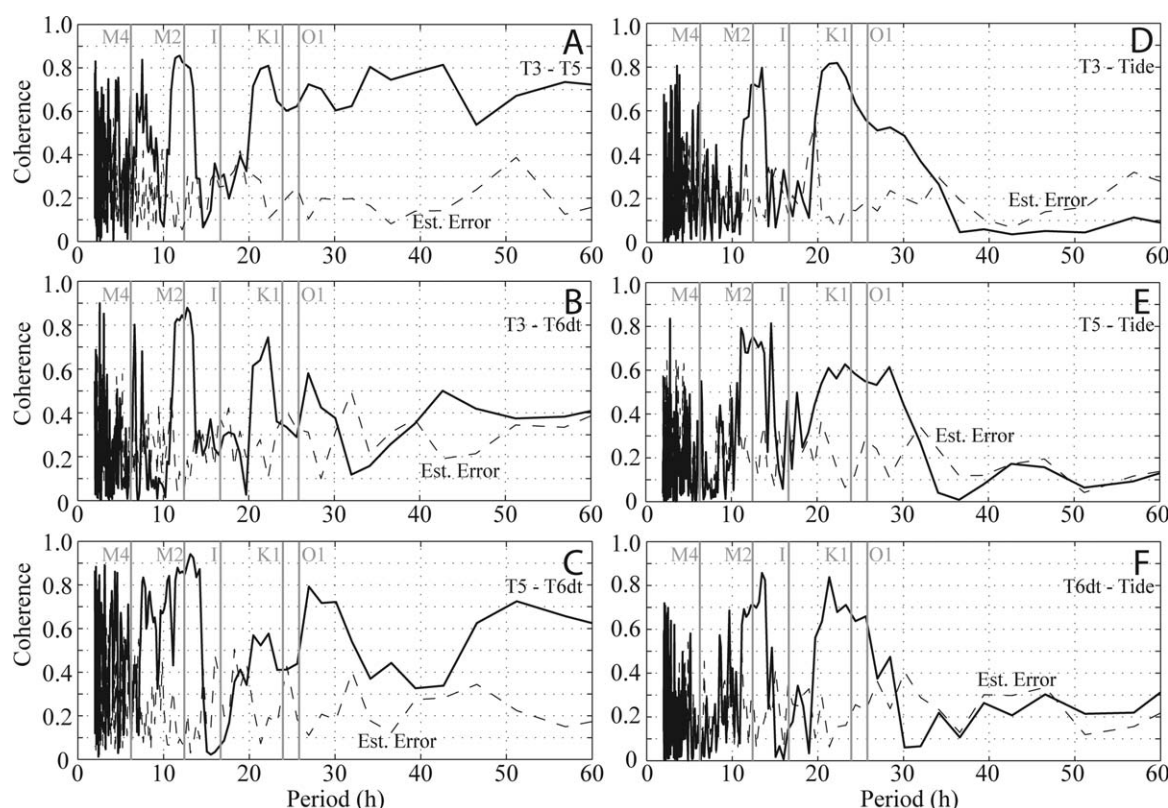| Values	Coherence	Phase Shift	$\pm$Error
T3-T5	0.82	$-12°$	10°
T3-T6dt	0.83	$-16°$	16°
T5-T6dt	0.85	3°	2°
T3-Tide	0.72	168°	10°
T5-Tide	0.75	173°	5°
T6dt-Tide	0.71	173°	8°

Figure 10. Coherence between (a–c) individual thermistors as a function of period show large values at the semidiurnal and, to a lesser degree diurnal periods, and variable coherence at short periods (<∼10 h). Coherence between T3 and T5 is large for diurnal and larger periods while T3–T6dt and T5–T6dt show lower values for these large periods. Coherence between the (D-E) thermistors and modeled tides show large peaks at the semidiurnal periods and, to a lesser degree, diurnal periods. Values of coherence are smaller at larger periods and highly variable at short periods (<∼10 h). Estimates of possible error in the coherence calculation are noted by dashed lines [*Barreyre et al.*, 2014b].

were calculated. Coherence values peak at the semidiurnal period (0.71–0.75; Table 2 and Figure 10) and broadly around the diurnal period (0.5–0.7; ∼20–30 h; Figure 10). At longer periods, coherence between temperature time series and tidal height is low and falls below the estimated errors. At shorter periods (∼1–3 h), close to the measurement interval of temperature data points, we observe some sharp peaks in coherence values. These peaks are likely associated with the measurement interval and not a physical relationship between tides and diffuse effluent temperature. Phase shifts between thermistor measurements are −12°, −16°, and 2 for thermistors 3 and 5, 3 and 6dt, and 5 and 6dt, respectively (Table 2). Estimated errors are approximately equal to the phase shifts suggesting nearly in phase variability, as expected for closely spaced temperature measurements. The phase shift between temperature time series and modeled tidal heights range from 168° to 173° with errors of 5° to 10° (Table 2). Thus, temperature variations are nearly completely out of phase with tidal pressure variations with probable lags of ∼0 to 45 min.

5. Discussion

5.1. Flow Modulation by Tidal Currents and Seafloor Pressure Variations

Previous studies of time-series measurements of diffuse venting temperatures and flow velocities observe peaks in power spectral density (PSD) at different periods, depending on the property in question and the geographical location. In 12 previous studies with sufficient temperature data to analyze periodic variations (Table 3), all find strong semidiurnal variability except for the study by *Pruis and Johnson* [2004]. In their 1998–1999 field study, the temperature PSD is nearly white for values measured inside a box cemented to the seafloor above a region of active diffuse venting at the Cracks vents in the southeast corner of the ASHES field. Only two of the above studies, both located on the TAG hydrothermal mound, find PSD peaks at diurnal periods in diffuse temperature data [*Kinoshita et al.*, 1998; *Sohn*, 2007]. In contrast with the nearly uniform observation of a semidiurnal tidal signal in time-series diffuse temperature data, three previous

Table 3. Variability of Diffuse Flow

Location	Duration	Quantities Measured*	Interpreted Spectral Peaks	Suggested Driving Mechanism
Guaymas Basin [*Little et al.*, 1988]	12 days	T	M2	Tidal currents
MEF [*Schultz et al.*, 1992]	44 days	T, V	None (V), M2 (T)	
TAG [*Kinoshita et al.*, 1996]	6 months	T, C	M2	
TAG [*Schultz et al.*, 1996]	7 days	T, V	M2, S2, N2 (T); O1, K1, P1 (V)	
TAG [*Kinoshita et al.*, 1998]	8 days	T	O1, M2	Tidal currents
Cleft [*Tivey et al.*, 2002]	5.5 months	T, C	M2, Inertial, 4–5 days	Tidal currents
ASHES [*Pruis and Johnson*, 2004]	206 days	T, V	None**	Tidal pressure
EPR [*Scheirer et al.*, 2006]	0.5–2 years	T, C	M2	Tidal currents
TAG [*Sohn*, 2007]	1 year	T	O1, M2, M3, M4	Tidal pressure
Lucky Strike [*Barreyre et al.*, 2014b]	Up to 3 years	T, C, P	M2, N2, K2	Tidal pressure and currents
Grotto (Main Endeavor) [*Lee et al.*, 2015]	8 months	T	O1, M2	Tidal pressure and currents
Grotto (Main Endeavor) [*Cuvelier et al.*, 2014]	23 days	T	12 h, 25 h	Tidal currents
ASHES (this study)	12 days	T, V	M2, 2-3 days***	Tidal pressure and currents

*T—temperature, V—velocities, C—current velocities, P—bottom pressure.
**Semidiurnal increases in flow variance were estimated to cause up to 5% changes in volume flux.
***2–3 day spectral peaks are only observed in temperature measurements from thermistors 6(dt) and 3.

studies with sufficient flow rate data for spectral analysis found a total absence of PSD peaks at the semi-diurnal period [*Pruis and Johnson*, 2004; *Schultz et al.*, 1992, 1996]. Despite the lack of spectral peaks, *Pruis and Johnson* [2004] do infer a semidiurnal variability in flow rates from narrow cracks located in the southeast portion of the ASHES field based upon daily increases in the variance of fluid velocities.

Analysis of flow rate data does show variability at diurnal periods. For example, *Schultz et al.* [1996] observe much greater power in the diffuse flow rate PSD at diurnal periods (O1, K1, and P1), than semidiurnal periods. In the current study, spectral peaks at semidiurnal periods occur in both temperature and flow rate measurements. Peaks at other periods are absent, however, except for periods of 2–3 days in data from thermistor 6 and for periods of ∼3 days from thermistor 3. In concert, the above observations of differing periodicity in diffuse venting at different sites are difficult to reconcile because measurement duration, sensing equipment, geographical location, and local tidal currents [e.g., *Sohn*, 2007] all may differ. It is clear that more extensive, careful observations and coincident measurements of diffuse flow rates and temperatures, concurrent with local current velocities and in situ tide measurements, are necessary. This would help to elucidate the variations in tidal influence on diffuse venting and the implications this periodicity may have for fluid circulation within the upper crust and its egress at diffuse venting sites.

The above studies attribute observed periodic variability to tidal currents, tidal pressure changes, or both. To distinguish between these sources, ideally we would compare our measurements to observations of both tidal pressure and bottom currents. Numerical models commonly predict the phase of tidal height variability with good accuracy, but tend to predict bottom currents with less accuracy. Given that no current velocity measurements exist for the ASHES vent field during the deployment of the DEMS system, we must rely on other data to constrain the role of tidally modulated pressure and currents on our measurements of diffuse venting.

The analyses of DEMS temperature and velocity measurements suggest that both currents and pressure are important controls on diffuse flow near the Phoenix vent, but that pressure effects may dominate. Evidence for tidal currents modulating the observed flow rates and temperatures includes flow being blown out of the image frame and altering the thermal boundary layer [e.g., *Scheirer et al.*, 2006], the spectral peaks at the 2–3 day period from thermistor 6dt and ∼3 day period from thermistor 3 that do not correlate with pressure variations, and the spectral peak at M2, which may be related to both pressure variations and tidal currents. Evidence for tidal pressure variations modulating observed flow rates and temperatures includes the M2 spectral peak, the lack of spectral peaks at M4 and at the inertial period, the high coherence of measured temperatures with modeled tidal height (0.7–0.75), and a phase lag that is approximately out of phase with the tides at M2, suggesting that high tides inhibit diffuse flow and low tides promote it, as expected for a tidal pumping scenario [e.g., *Davis and Becker*, 1999; *Sohn*, 2007]. Additionally, *Prius and*

Johnson [2004] determined that some variability is associated with tidal pressure variations at the ASHES field based on previous diffuse flow rate and temperature measurements that were isolated from bottom currents. Finally, there is no significant correlation between upwelling velocity of diffuse flow and the lateral velocity imposed by currents ($R^2 = 0.056$; supporting information Figure S6). If stronger currents cause flow to decrease, one would expect a negative correlation between lateral and vertical velocities, despite gaps in flow measurements during the strongest bottom currents.

The above results suggest a strong connection between flow variability and tidal pressure variations at the seafloor, but it is possible that gaps in the DEMS velocity measurements during the strongest currents introduce a bias in our calculations. However, our analysis included records that extend uninterrupted over numerous tidal cycles (up to 34 h; supporting information Figure S1), which should capture the effect of bottom currents on flow, therefore we believe that data gaps have limited influence on our results. One caveat is that tidal variability with periods of several days, such as some current components observed along the Endeavour segment [e.g., *Thomson et al.*, 2003], may not be well resolved for some data gaps. We do not observe these periods of current variation in our temperature data, but cannot completely rule out an effect on flow rates.

5.2. Comparison of Diffuse Heat Output to Previous Estimates

Rona and Trivett [1992] estimate the total heat output from the ASHES hydrothermal field to be 49 ± 32 MW, with 4.4 ± 2.2MW from high-temperature, focused flow, and the remaining heat output from diffuse venting (45 ± 30 MW). Based on analyses of the photo mosaic of the ASHES field as it existed in 2010 [*Kelley et al.*, 2014], and our 2014 estimate of diffuse heat flux 0.29 ± 0.22 MW m^{-2}, we find a diffuse heat output emanating from fractures of 2.05 ± 1.95 MW (section 4.4). This calculation indicates that the diffuse heat output due to narrow cracks at the ASHES field is between $<1\%$ and 24% of the total diffuse heat output, with the remainder coming from patches, wide cracks, and sulfide mounds or towers. Although the overall heat output may have changed since the estimates by *Rona and Trivett* [1992], we use their values here because there are no other available estimates for the ASHES vent field.

Using these estimates, we examine the fraction of diffuse flow due to narrow cracks at ASHES relative to those previously calculated over the entire Lucky Strike hydrothermal field (Mid-Atlantic Ridge at $\sim37°$N), and at the individual vent sites of Tour Eiffel and Y3 within the Lucky Strike field [*Barreyre et al.*, 2012; *Mittelstaedt et al.*, 2012]. The Lucky Strike vent field is located within the summit of an on-axis volcano that occupies a large area within the ~14 km-wide rift valley of the Mid-Atlantic Ridge, approximately 400 km southwest of the Azores Islands. The vent field covers an area ~1 km^2 and emits a total diffuse heat output of 612 ± 424 MW [*Barreyre et al.*, 2012]. Within the Lucky Strike field, the Tour Eiffel vent site emits a diffuse heat output of 18.75 ± 2.2 MW [*Mittelstaedt et al.*, 2012] from an area ~30 m $\times$ ~50 m (1500 m^2), equivalent to $\sim40\%$ the area of the ASHES vent field (~60 m $\times$ ~60 m = 3600 m^2). The Y3 vent site is slightly smaller than Tour Eiffel at ~30 m $\times$ ~40 m (1200 m^2), but emits a statistically identical diffuse heat output of 13.9 ± 6.6 MW [*Mittelstaedt et al.*, 2012].

Examining the diffuse flow around the Tour Eiffel and Y3 vents, *Mittelstaedt et al.* [2012] estimate that the fraction of the total diffuse heat output due to thin cracks at each vent is $\sim16\%$ and $\sim67\%$, respectively. For the entire Lucky Strike field, cracks are estimated to contribute $\sim43\%$ of the total diffuse heat output [*Barreyre et al.*, 2012]. Based upon these estimates and our value for ASHES, there does not appear to be a correlation between diffuse heat output due to narrow cracks and the overall spatial area of a vent field or its total diffuse heat output. Both Y3 and Tour Eiffel are smaller than the ASHES field and emit a diffuse heat output that is on the low end of the estimates for ASHES [*Rona and Trivett*, 1992], but the fraction of this heat output due to narrow cracks differs significantly between them. Narrow cracks around Tour Eiffel emit a fraction of diffuse heat output similar to the ASHES field, but narrow cracks around Y3 emit a much higher fraction.

The local permeability structure and subsurface hydrothermal circulation patterns are likely the primary controls on the fraction of diffuse heat output due to narrow cracks, separate from that due to other diffuse venting types. The above comparison highlights the importance of obtaining detailed field coverage of all types of diffuse venting on a per-site basis to achieve accurate estimates of the total diffuse heat output; extrapolation from a single vent site without other constraints (e.g., a photo mosaic or detailed video coverage) will incur unreasonable errors.

5.3. Controls on Diffuse Venting

Previous studies have examined relationships between high-temperature MOR hydrothermal venting and several geologic factors such as the presence and depth of an axial magma chamber (AMC), the proximity to high permeability structures (e.g., faults, fractures, and drainback features), and the rate of extrusive volcanism [e.g., *Baker*, 2009; *Barreyre et al.*, 2012; *Fornari et al.*, 2004; *German et al.*, 1994; *Mittelstaedt et al.*, 2012]. These geological and spatial relationships clearly influence the locations of vents and vent fields and their overall heat output, but much remains to be understood about both global MOR heat output and the processes controlling it. *Baker* [2009] used plume incidence measurements to argue that nearly all high-temperature vent fields directly overlie AMCs (37 out of 40 studied), and that the intensity of high-temperature venting increases as depth to the AMC decreases, suggesting a link between hydrothermal heat flux and depth to the driving heat source. In contrast, *Lowell et al.* [2013] plot available measured heat output data versus depth to magma chambers and find no correlation. At the seafloor, the locations of discrete, high-temperature vents are highly correlated with faults, fractures, and areas of lava drainback above primary eruptive volcanic fissures [*Kent et al.*, 1993; *Barreryre et al.*, 2012; *Fornari et al.*, 2004], demonstrating a link between open, high-permeability conduits in the upper crust and high-temperature vent formation. Diffuse flow rates also appear to be controlled by variations in the near surface permeability field; within a single field rates of fluid flow are highest at fractures in the surface basalt [e.g., *Mittelstaedt et al.*, 2012]. Indeed, the widespread fracture network of ASHES measured here, as well as the flow measured by the DEMS, which exits a small fracture, suggest that variations in shallow permeability strongly influence diffuse flow at the ASHES vent field too. Although several observations exist of geologic influences on the locations and overall intensity of high-temperature hydrothermal vents, the hydrogeology of the shallowest crust (<500 m) and how its architecture may influence diffuse heat fluxes and the ratio of diffuse to discrete heat flux remains poorly constrained.

One significant barrier to understanding diffuse venting and, thus, shallow crustal permeability structure, is the role of conductive heat transfer in driving convective flow in the thermal boundary layer just above the seafloor. Conductively driven flow will have a similar appearance (shimmering water) to diffuse effluent exiting the seafloor. In this study, we examine diffuse flow from a small fracture in a basaltic sheet flow, the magnitude of flow variability, and the phase lag of diffuse flow relative to tidal forcing. Three lines of evidence suggest that the flow rate variability measured by the DEMS is not driven by conductive heat transport: (1) the fluid flow is very localized with little to no flow visible above the immediately surrounding seafloor, (2) the observed phase lags can only be reproduced for an impermeable layer <~10cm thick, and (3) the temperature gradient required to match the observed heat flux implies unreasonable subsurface temperatures (>500°C) if the layer thickness is >~0.5 cm. First, the restricted nature of the flow field suggests that heat is not diffusing throughout the surface rock layer; diffusion of heat from a subsurface reservoir would lead to a wide area of warm seafloor and, thus, a wide distribution of convective diffuse motions. Second, we use a finite-difference solution of the conduction equation to estimate the phase lag between changes in subsurface temperature (presumably driven by semidiurnal tidal cycles) and the resultant change in heat flux delivered to the surface (see caption of supporting information Figure S7 for model details). For impermeable basalt thicknesses of 1–50 cm, we predict that the layer thickness must by <~10cm to match the maximum observed phase lag of ~45m (supporting information Figure S7a); smaller phase lags require thinner layers. Third, if the observed heat flux (0.29 MW m^{-2}) is delivered to the surface by conduction, it implies a mean temperature gradient that depends upon the layer thickness through Fourier's law, q $= -k(dT/dz)$, where z is the vertical coordinate, and k is thermal conductivity of basalt (3.3 W m^{-1} K^{-1}, supporting information Figure S7b); only layer thicknesses <~0.5 cm yield subsurface temperatures <500°C, much warmer than predicted to exist 0.5 cm beneath the surface [e.g., *Lowell et al.*, 2015]. Taken together, these pieces of evidence strongly indicate that the flow measured by the DEMS was driven by subsurface pressure gradients and not conductive heating of near-surface seawater.

5.4. Evaluation of the DEMS and Future Improvements

The DEMS is a new, deep-sea camera system that successfully captured imagery and thermistor readings that allowed minimally-invasive measurements of temperature and velocity to be made of diffuse effluent rising from a seafloor fracture for ~12 days. Thermistors 3, 5, and 6 measured highly coherent temperature patterns both between thermistors and relative to tidal height variations. Several previous studies observe semidiurnal variations in either temperature or velocity measurements of diffuse flow (Table 3). However,

we are unaware of another study of diffuse venting that observes the semidiurnal tidal (M2) peak in coregistered temperatures and velocities.

The estimated errors on the average heat flux and heat output presented here include both measurement error, as well as real variance in the flow rates and temperatures. To evaluate the performance of the DEMS system, it is important to note the differences between each contribution to the estimated errors. The DEMS system is designed to make accurate measurements of velocity (error ∼5–7%, [*Mittelstaedt et al.*, 2010]) and temperature (error ∼±0.1°C) over recurring data capture periods. During each period, the system measured velocities every 0.05s and temperatures every second. These rapid measurements are very effective at capturing short-term (e.g., 20 s) changes in flow rate and effluent temperatures. Estimated errors associated with the spatial and temporal averaging of velocities and temperatures include both the measurement errors and the flow variance. For this reason, DEMS data result in estimates of the average heat flux with similar error ranges to previous methods, but errors on the temporal evolution of flow are smaller. Thus, as currently configured, the DEMS is ideal for measuring the temporal variability of diffuse flow at a given location.

The successful test of this system also indicates several areas of potential improvements to the instrumentation. The thermistors and thermistor housings need to be reevaluated to determine the cause of failures in thermistors 1, 2, and 4. In addition, thermistor housings need to be better protected from direct contact with upwelling flow as this may have contributed to observed long-term temperature trends in thermistor 6. Replicate thermistors and perhaps additional ones embedded within the panel structure may be possible in future redesigns of the system. Beyond improvements to the thermistors, the loss of data during times of high current velocities causes difficulties when performing spectral analysis. One solution may be to redesign the frame of the DEMS so that the camera and thermistors are closer to the seafloor. This may be facilitated by a reduction in the system footprint, which can be accomplished by changing from lead-acid to lithium-ion batteries. A second solution to the problem of strong currents would be to block lateral flow into and out of the region between the camera and image board, but this would remove the effect of bottom currents on flow rates and temperatures, thereby introducing a different aliasing mechanism. Finally, future DEMS deployments must include an attached or nearby current meter to properly assess the degree to which bottom currents modulate flow rates. Incorporating these changes into a future version of the DEMS will reduce its size and simultaneously increase its reliability, efficacy, and accuracy of its measurements.

6. Conclusions

This study reports results from a new, deep-sea digital camera system designed to collect time-series temperature and velocity measurements of diffuse hydrothermal effluent exiting the seafloor. The DEMS collects images of upwelling diffuse flow passing between a camera and a fixed background pattern. Velocities are calculated from this imagery using DFV, a noninvasive cross-correlation method to calculate the motion of index of refraction anomalies (hot fluids) [*Mittelstaedt et al.*, 2010]. Six thermistors, with three above and three below the image board, record temperatures as fluids rise into and exit out of the camera image frame. The DEMS was deployed above a narrow crack located ∼10 m southeast of the Phoenix vent along the southern edge of the ASHES vent field, within Axial Seamount's caldera on the Juan de Fuca Ridge. During the ∼12 day deployment, the DEMS successfully recorded temperatures using 3 of the 6 thermistors and imagery for velocity calculations once per hour for ∼24 s at rates of 1 Hz and 20 Hz, respectively. Results of this study demonstrate the DEMS's ability to autonomously capture time-series measurements, which permit calculations of the volume and heat flux of diffuse hydrothermal fluids.

Measurements of diffuse effluent rising from a narrow crack near the Phoenix vent yield a range of measured velocity and temperature values. Vertical velocities range between 0.1 and 5.8 cm s^{-1} for fluids with temperatures between 2.1°C and 4.1°C (thermistor 5). Normalized power spectra of all temperature and velocity time-series show a strong semidiurnal peak at the M2 tidal period. Other spectral peaks are absent except in data from thermistor 6dt and 3, which have an additional peak at 2–3 day periods. We attribute this periodic variability to both bottom currents and changes in pressure associated with tidal height variations, but conclude that pressure variations likely dominate changes in temperature and velocity.

Time-series data in conjunction with analyses of imagery from the *Alvin* submersible and a 2010 photo mosaic of the ASHES field [*Kelley et al.*, 2014] were used calculate the heat flux for a narrow crack beneath the DEMS, and to extrapolate that estimate of the heat flux due to narrow cracks across the entire ASHES field. Flow from the narrow crack measured by the DEMS has a time averaged heat flux over the period of measurement of 0.29 ± 0.22 MW m^{-2} and a heat output of 3.1 ± 2.5 kW. Using the photo mosaic to measure the length and a statistical sample of the widths of narrow cracks across the ASHES field, narrow cracks have an estimated total heat output of 2.05 ± 1.95 MW. This suggests that the heat output due to narrow cracks is <1%–24% of the total diffuse heat output of the ASHES field. Comparing this value to previous estimates at the Lucky Strike hydrothermal field, we find that the fraction of diffuse heat output due to narrow cracks varies significantly between individual vents and between vent fields. We interpret these results to indicate that the local permeability structure likely controls the pervasiveness of thin cracks relative to other diffuse venting sources on mid-ocean ridges at different spreading rates. However, the range of values may also reflect the small number and inaccuracy of existing estimates. Given the importance of properly constraining mid-ocean ridge heat output into the bottom water of the global ocean, more experiments with improved capabilities like the DEMS should be conducted at a wide range of mid-ocean ridge vent sites.

References

Baker, E. T. (2009), Relationships between hydrothermal activity and axial magma chamber distribution, depth, and melt content, *Geochem. Geophys. Geosyst.*, *10*, Q06009, doi:10.1029/2009GC002424.

Barreyre, T., and R. Sohn (2016), Poroelastic response of mid-ocean ridge hydrothermal systems to ocean tidal loading: Implications for shallow permeability structure, *Geophys. Res. Lett.*, *43*, 1660–1668, doi:10.1002/2015GL066479.

Barreyre, T., J. Escartin, R. Garcia, M. Cannat, E. Mittelstaedt, and R. Prados (2012), Structure, temporal evolution, and heat flux estimates from the Lucky Strike deep-sea hydrothermal field derived from seafloor image mosaics, *Geochem. Geophys. Geosyst.*, *13*, Q04007, doi:10.1029/2011GC003990.

Barreyre, T., J. Escartin, R. Sohn, and M. Cannat (2014a), Permeability of the Lucky Strike deep-sea hydrothermal system: Constraints from the poroelastic response to ocean tidal loading, *Earth Planet. Sci. Lett.*, *408*, 146–154.

Barreyre, T., J. Escartin, R. Sohn, M. Cannat, V. Ballu, and W. C. Crawford (2014b), Temporal variability and tidal modulation of hydrothermal exit-fluid temperatures at the Lucky Strike deep-sea vent field, Mid-Atlantic Ridge, *J. Geophys. Res. Solid Earth*, *119*, 2543–2566, doi:10.1002/2013JB010478.

Bemis K., R. P. Lowell, and A. Farough (2012), Diffuse flow on and around hydrothermal vents at mid-ocean ridges, *Oceanography*, *25*(1), 182–191.

Bird, P. (2003) An updated digital model of plate boundaries, *Geochem. Geophys. Geosyst.*, *4*(3), 1027, doi:10.1029/2001GC000252.

Butterfield, D. A., et al. (1990), Geochemistry of hydrothermal fluids from Axial seamount hydrothermal emissions study vent field, Juan de Fuca Ridge: Subseafloor boiling and subsequent fluid-rock interaction, *J. Geophys. Res.*, *95*(B8), 12895–12,921.

Butterfield, D. A., et al. (2004), Mixing, reaction and microbial activity in the sub-seafloor revealed by temporal and spatial variation in diffuse flow vents at Axial Volcano, in *The Subseafloor Biosphere at Mid-Ocean Ridges, Geophys. Monogr. Ser.*, vol. 144, pp.269–290, W. S. Wilcock et al., AGU, Washington, D. C.

Canales, J. P., S. C. Singh, R. S. Detrick, S. M. Carbotte, A. J. Harding, G. M. Kent, J. B. Diebold, J. M. Babcock, and M. R. Nedimovic (2006), Seismic evidence for variations in axial magma chamber properties along the southern Juan de Fuca Ridge, *Earth Planet. Sci. Lett.*, *246*, 353–366.

Chadwick, W., R. Embley, D. Clague, and D. Butterfield (2015), Processed Swath Bathymetry Grids (NetCDF:GMT format) Derived From Multibeam Sonar Data From the Juan de Fuca: Axial Seamount Assembled as part of the JdF_Gorda:NOAA_VENTS Data Compilation, Integrated Earth Data Applications (IEDA), Mar. Geosci. Data Cent., doi:10.1594/IEDA/317691.

Cherkaoui, A. S. M., W. S. D. Wilcock, R. Dunn, and D. R. Toomey (2003), A numerical model of hydrothermal cooling and crustal accretion at a fast spreading mid-ocean ridge, *Geochem. Geophys. Geosyst.*, *4*(9), 8616, doi:10.1029/2001GC000215.

Crone, T. J., W. S. D. Wilcock, and R. E. McDuff (2010), Flow rate perturbations in a black smoker hydrothermal vent in response to a mid-ocean ridge earthquake swarm, *Geochem. Geophys. Geosyst.*, *11*, Q03012, doi:10.1029/2009GC002926.

Crone, T. J., E. Mittelstaedt, and D. Fornari (2014), Using the VentCam and optical plume velocimetry to measure high-temperature hydrothermal fluid flow rates in the ASHES vent field on Axial Volcano, Abstract #V12B-07presented at 2014 Fall Meeting, AGU, San Francisco, Calif., 15–19 Dec.

Cuvelier D., P. Legendre, A. Laes, P.-M. Sarradin, and J. Sarrazin (2014) Rhythms and community dynamics of a hydrothermal tubeworm assemblage at main endeavour field: A multidisciplinary deep-sea observatory approach, *PLoS One*, *9*(5), e96924, doi:10.1371/journal.pone.0096924.

Davis, E., and K. Becker (1999), Tidal pumping of fluids within and from the oceanic crust: New observations and opportunities for sampling the crustal hydrosphere, *Earth Planet. Sci. Lett.*, *172*, 141–149.

Di Iorio, D., J. W. Lavelle, P. A. Rona, K. Bemis, G. Xu, L. N. Germanovich, R. P. Lowell, and G. Genc (2012) Measurements and models of heat flux and plumes, *Oceanography*, *25*(1), 182–191.

Dziak, R. P., S. R. Hammond, and C. G. Fox (2011), A 20-year hydroacoustic time series of seismic and volcanic events in the Northeast Pacific Ocean, *Oceanography*, *24*(3), 280–293, doi:10.5670/oceanog.2011.79.

Elderfield, H., and A. Schultz (1996), Mid-ocean ridge hydrothermal fluxes and the chemical composition of the ocean, *Annu. Rev. Earth Planet. Sci.*, *24*, 191–224.

Escartin, J., G. Hirth, and B. Evans (1997), Effects of serpentinization on the lithospheric strength and the style of normal faulting at slow-spreading ridges, *Earth Planet. Sci. Lett.*, *151*, 181–189.

Fornari, D. J., et al. (2004), Submarine lava flow emplacement at the East Pacific Rise 9o50'N: Implications for uppermost ocean crust stratigraphy and hydrothermal fluid circulation, in *Mid-Ocean Ridges: Hydrothermal Interactions Between Lithosphere and Oceans*, edited by C. German et al., AGU, Washington, D. C.

Fornari, D. J., et al. (2012) The East Pacific Rise between 9°N and 10°N: Twenty-five years of integrated, multidisciplinary oceanic spreading center studies. *Oceanography*, *25*(1), 18–43, doi:10.5670/oceanog.2012.02.

Fujioka, K., K. Kobayashi, and A. Nishizawa (1997), Tide-related variability of TAG hydrothermal activity observed by deep-sea monitoring system and OBSH, *Earth Planet. Sci. Lett.*, *153*, 239–244.

German, C., et al. (1994), Hydrothermal activity on the Reykjanes Ridge: The Steinaholl vent-field at 63o06'N, *Earth Planet. Sci. Lett.*, *121*, 647–654.

Germanovich, L. N., R. S. Hurt, J. E. Smith, G. Genc, and R. P. Lowell (2015), Measuring fluid flow and heat output in seafloor hydrothermal environments, *J. Geophys. Res. Solid Earth*, *120*, 8031–8055, doi:10.1002/2015JB012245.

Ginster, U., M. J. Mottl, and R. P. Von Herzen (1994), Heat flux from black smokers on the Endeavour and Cleft segments, Juan de Fuca Ridge, *J. Geophys. Res.*, *99*(B3), 4937–4950.

Kelley, D. S., J. R. Delaney, and S. K. Juniper (2014), Establishing a new era of submarine volcanic observatories: Cabling Axial Seamount and the Endeavour Segment of the Juan de Fuca Ridge, *Mar. Geol.*, *352*, 426–450, doi:10.1016/j.margeo.2014.1003.1010.

Kinoshita, M., O. Matsubayashi, and R. P. Von Herzen (1996), Sub-bottom temperature anomalies detected by long-term temperature monitoring at the TAG hydrothermal mound, *Geophys. Res. Lett.*, *23*, pp. 3467–3470.

Kinoshita, M., R. P. Von Herzen, O. Matsubayashi, and K. Fujioka (1998), Tidally-driven effluent detected by long-term temperature monitoring at the TAG hydrothermal mound, Mid-Atlantic Ridge, *Phys. Earth Planet. Inter.*, *108*, 143–154.

Lee, R. W., K. Robert, M. Matabos, A. E. Bates, and S. K. Juniper (2015) Temporal and spatial variation in temperature experienced by macrofauna at Main Endeavour hydrothermal vent field, *Deep-Sea Res., Part I*, *106*, 154–166 doi:10.1016/j.dsr.2015.10.004.

Little, S. A., K. Stolzenback, and F. J. Grassle (1988), Tidal current effects on temperature in diffuse hydrothermal flow: Guaymas Basin, *Geophys. Res. Lett.*, *15*(13), 1491–1494.

Lomb, N. R. (1976), Least-squares frequency analysis of unequally spaced data, *Astrophys. Space Sci.*, *39*(2), 447–462.

Lowell, R. P., A. Farough, L. N. Germanovich, L. B. Hebert, and R. Horne (2012) A vent-field-scale model of the East Pacific Rise 9°50'N magma-hydrothermal system, *Oceanography*, *25*(1), 182–191.

Lowell, R. P., A. Farough, J. Hoover, and K. Cummings (2013), Characteristics of magma-driven hydrothermal systems at oceanic spreading centers, *Geochem. Geophys. Geosys.*, *14*, 1756–1770, doi:10.1002/ggge20109.

Lowell, R. P., J. L. Houghton, A. Farough, K. L. Craft, B. I. Larson, and C. D. Meile (2015), Mathematical modeling of diffuse flow in seafloor hydrothermal systems: The potential extent of the subsurface biosphere at mid-ocean ridges, *Earth Planet. Sci. Lett.*, *425*, 145–153.

Lutz, R. A., et al. (2008), Interrelationships between vent fluid chemistry, temperature, seismic activity, and biological community structure at a mussel-dominated, deep-sea hydrothermal vent along the East Pacific Rise, *J. Shellfish Res.*, *27*(1), 177–190.

Malahoff, A., G. McMurtry, S. Hammond, and R. W. Embley (1984), High-temperature hydrothermal fields—Juan de Fuca Ridge—Axial Volcano, *Eos Trans. AGU*, *65*, 1112.

Matsumoto, K., T. Takanezawa, and M. Ooe (2000), Ocean tide models developed by assimilating TOPEX/POSEIDON altimeter data into hydrodynamical model: A global model and a regional model around Japan, *J. Oceanogr.*, *56*, 567–581.

Mittelstaedt, E., A. Davaille, P. E. van Keken, N. Gracias, and J. Escartin (2010), A noninvasive method for measuring the velocity of diffuse hydrothermal flow by tracking moving refractive index anomalies, *Geochem. Geophys. Geosyst.*, *11*, Q10005, doi:10.1029/2010GC003227.

Mittelstaedt, E., J. Escartin, N. Gracias, J.-A. Olive, T. Barreyre, A. Davaille, M. Cannat, and R. Garcia (2012), Quantifying Diffuse versus discrete venting at the Tour Eiffel vent site, Lucky Strike hydrothermal field, *Geochem. Geophys. Geosyst.*, *13*, Q04008, doi:10.1029/2011GC003991.

Nees, H. A., T. S. Moore, K. M. Mullaugh, R. R. Holyoke, C. P. Janzen, S. Ma, E. Metzger, T. J. Waite, M. Yucel, and R. A. Lutz (2008), Hydrothermal vent mussel habitat chemistry, pre- and post-eruption at 9o50 North on the East Pacific Rise, *J. Shellfish Res.*, *27*(1), 169–175.

Percival, D., and A. Walden (1993), *Spectral Analysis for Physical Applications*, Cambridge Univ. Press, Cambridge.

Press, W. H., S. A. Teukolsky, W. T. Vetterling, and B. P. Flannery (2002), *Numerical Recipes in C++*, Cambridge Univ. Press, Cambridge.

Pruis, M. J., and H. P. Johnson (2004), Tapping into the sub-seafloor: Examining diffuse flow and temperature from an active seamount on the Juan de Fuca Ridge, *Earth Planet. Sci. Lett.*, *217*, 379–388.

Ramondenc, P., L. N. Germanovich, K. L. Von Damm, and R. P. Lowell (2006), The first measurements of hydrothermal heat output at 9°50'N, East Pacific Rise, *Earth Planet. Sci. Lett.*, *245*, 487–497, doi:10.1016/j.epsl.2006.03.023.

Rona, P. A., and D. A. Trivett (1992), Discrete and diffuse heat transfer at ASHES vent field, Axial Volcano, Juan de Fuca Ridge, *Earth Planet. Sci. Lett.*, *109*, 57–71.

Scargle, J. D. (1982), Studies in astronomical time series analysis II: Statistical aspects of spectral analysis of unevenly spaced data, *Astrophys. J.*, *263*, 835–853.

Scheirer, D. S., T. M. Shank, and D. J. Fornari (2006), Temperature variations at diffuse and focused flow hydrothermal vent sites along the northern East Pacific Rise, *Geochem. Geophys. Geosyst.*, *7*, Q03002, doi:10.1029/2005GC001094.

Schultz, A., J. R. Delaney, and R. E. McDuff (1992), On the partitioning of heat flux between diffuse and point source seafloor venting, *J. Geophys. Res.*, *97*(B9), 12,299–12,314.

Schultz, A., P. Dickson, and H. Elderfield (1996), Temporal variations in diffuse hydrothermal flow at TAG, *Geophys. Res. Lett.*, *23*(23), 3471–3474.

Sohn, R. A., Webb, S. C., Hildebrand, J. A. (2004), Fine-scale seismic structure of the shallow volcanic crust on the East Pacific Rise at 9–50'N, *J. Geophys. Res.*, *109*, B12104, doi:10.1029/2004JB003152.

Thompson, D. J. (1982), Spectrum estimates and harmonic analysis, *Proc. IEEE*, *70*, 1055–1096.

Thomson, R. E., S. F. Milhaly, A. B. Rabinovich, R. E. McDuff, S. R. Veirs, and F. R. Stahr (2003), Constrained circulation at Endeavour ridge facilitates colonization by vent larvae, *Nature*, *424*, 545–549.

Tivey, M. A., A. Bradley, T. M. Joyce, and D. Kadko (2002), Insights into tide-related variability at seafloor hydrothermal vents from time-series temperature measurements, *Earth Planet. Sci. Lett.*, *202*, 693–707.

Von Damm, K. L., and M. Lilley (2004), Diffuse flow hydrothermal fluids from 9o50'N East Pacific Rise: Origin, evolution and biogeochemical controls, in *The Subseafloor Biosphere at Mid-Ocean Ridges*, edited by W. S. D. Wilcock, et al., AGU, Washington, D. C.

Westerweel, J. (1997), Fundamentals of digital particle image velocimetry, *Meas. Sci. Technol.*, *8*(12), 1379–1392.

Willert, C. E., and M. Gharib (1991), Digital particle image velocimetry, *Exp. Fluids*, *10*, 181–193.